Chapter 5

An ANNNXY model for transversely polarized achiral smectics

5.1 Introduction

In the previous chapters, we have seen that the chirality of the medium plays an important role in the realization of transverse electric polarization in the tilted smectic liquid crystalline phases. As the medium can not be more symmetric than any of its macroscopic properties, the maximum symmetry allowed for a medium to sustain electric polarization is $C_{\infty v}$ which is the symmetry of a proper vector. Chirality of the molecules reduces the symmetry C_{2h} of the tilted SmC layers to C_2 by removing the mirror plane perpendicular to the C_2 axis. This reduced symmetry (lower than $C_{\infty v}$) of the resulting SmC* layers allows them to be polarized.

However, a polar symmetry of the system does not require the medium to be chiral. The necessary condition for the medium to have electric polarization is that it has a symmetry lower than $C_{\infty v}$. For this reason, a great deal of attention has been directed, both theoretically and experimentally, towards the realization of an achiral ferroelectric liquid crystalline system. The possibility of a polarized 3-d liquid (polar nematic) has been the subject of a large number of theoretical discussions [57]. There appears to be no experimental realization of such a medium upto now. The SmA phase itself is uniaxial if the molecules can freely rotate about their long axes. It may be thought that molecules with longitudinal dipoles can form a ferroelectric SmA with the polarization along the layer normal (longitudinal ferroelectricity). Actually, such compounds with molecules having large dipole moments along the long axes are found to exhibit an anti-parallel near neighbour orientation of the dipoles in successive layers giving rise to the so called longitudinal antiferroelectric SmA phase. In addition these materials also exhibit a variety of other sub-phases of the SmA [27] phase. More recently, the possibility of longitudinal ferroelectricity exhibited by polyphilic molecules with 3 or 4 different chemical subgroups has been discussed [58], and indeed an experimental evidence for a relatively weakly polarized SmA consisting of achiral polyphilic molecules was claimed to have been
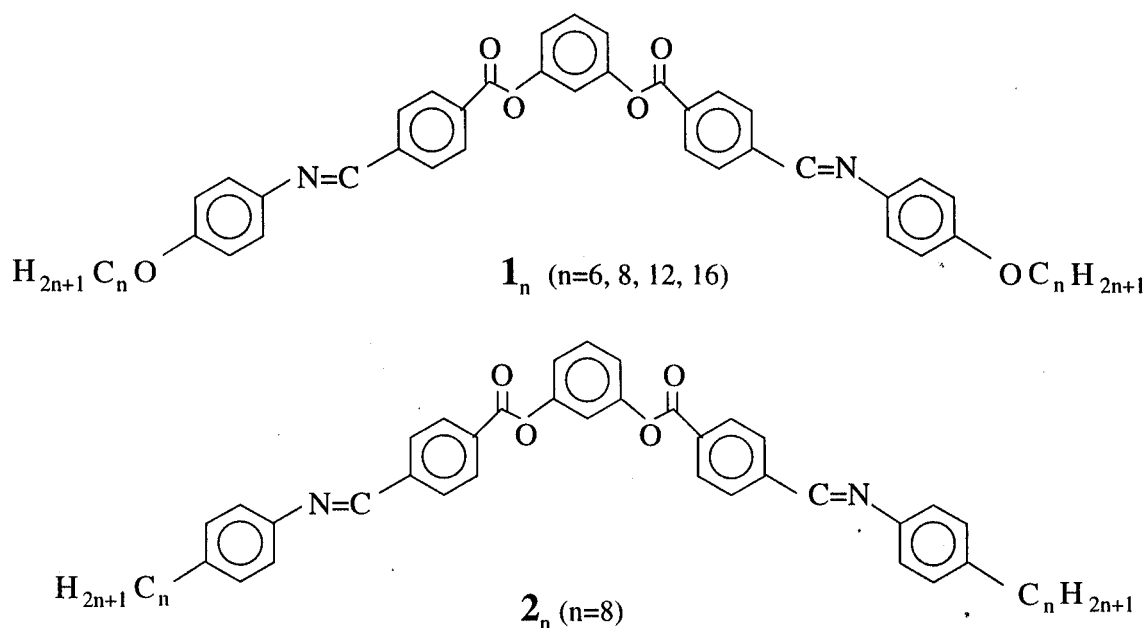
Fig. 5.1: The molecular structures of the achiral bent banana shaped molecules exhibiting the smectic phases with transversely polarized layers.

found [59]. However, very recently careful studies [60] have shown that it is also an antiferroelectric medium.

If the molecules themselves have strong biaxiality, one can get a biaxial SmA phase. Recently, Niori *et al.* [25] have synthesized some compounds with bent banana shaped *achiral* molecules which are found to exhibit smectic phases. The molecular structures of such bent molecules are shown in Fig. 5.1. The corresponding phase sequences exhibited by different homologs of these compounds are shown in table 5.1. The smectic phases exhibited by such molecules are quite interesting because of the characteristic shape of the molecules. In each layer the banana shaped molecules are closely packed and are all aligned with their bending directions on the average parallel to each other (see Fig. 5.2). Therefore, each layer is biaxial with the refractive indicatrix being a triaxial ellipsoid. The maximum principal refractive index is along the layer normal (z-axis). The other two principal axes of the refractive indicatrix are in the plane of the layer. The intermediate principal refractive index is along the direction in which the bending directions of the molecules are aligned (x-axis). The point symmetry of the layer is represented by the C_{2v} group. There is a two-fold axis along the x-axis and two mirror planes perpendicular to y and z axes. Since the symmetry of the layer is lower than $C_{\infty v}$ and there is no mirror plane perpendicular to the two-fold axis, spontaneous electric polarization can be expected to arise along the x-axis. In fact Niori *et al.* [26] could measure a spontaneous polarization in some phases exhibited by the compounds synthesized by them using the polarization reversal current obtained on applying a triangular wave voltage. They found the transverse polarization of the medium to be ≈ 60 nC/cm^2. More interestingly, even in this *achiral* system, they have found a *helicoidal* structure in which the polarization

	Iso.		SmX$_1$		SmX$_2$		SmX$_3$
1$_6$	●	176° C	●	172° C	●	159° C	●(h)
	●	174° C	●	158° C	●	146° C	●(h)
1$_8$	●	176° C	●(h)	163° C	●	157° C	●(h)
	●	173° C	●(h)	152° C	●	141° C	●(h)
1$_{12}$	●	172° C	●(h)	149° C	−		●(h)
	●	169° C	●(h)	142° C	−		●(h)
1$_{16}$	●	163° C	●(h)	143° C	−		●(h)
	●	161° C	●(h)	138° C	−		●(h)
2$_8$	●	161° C	●(h)	155° C	●	96° C	−
	●	157° C	●(h)	138° C	●	73" C	−

Table **5.1:** The phase sequences of the different homologs of the bent molecules. The crystalline phase below SmX$_3$ is not shown in the table. (h) indicates the presence of helical structure.
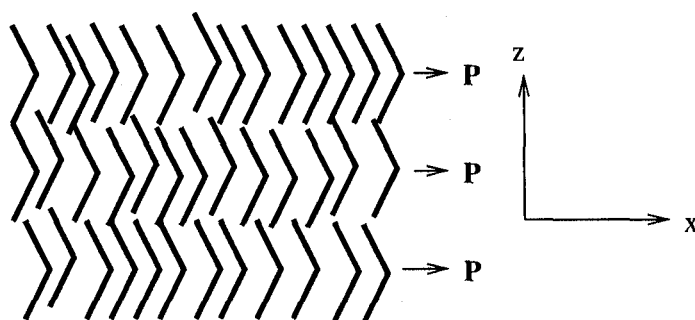

Fig. **5.2:** Schematic diagram of the smectic phase with transversely polarized layers exhibited by compounds with bent molecules.

precesses along the layer normal in the ferroelectric state.

In this chapter we will discuss theoretically the phase transitions and the origin of spontaneous helical structures in these novel liquid crystalline systems. We will show that the helical structures are stabilized by the competing interactions of the nearest and next nearest neighbour layers and the sense of the helix can be either right handed or left handed as it results from a spontaneous breaking of the chiral symmetry.

The stabilization of this type of modulated structure by competing interactions is known in magnetic materials. In some magnetic crystalline systems, it is found that the interaction between the spins in a certain plane (xy-plane) is ferromagnetic in nature, whereas in the orthogonal direction (z), an antiferromagnetic interaction between the next nearest neighbouring spins competes with the nearest neighbour (NN) interaction. The axial next nearest neighbour xy model (ANNNXY) can be invoked to describe the phase transitions in such systems assuming that the 2-d classical spins lie in the xy-plane [39]. The interaction along the z-direction is usually modeled as $-J_1 \vec{S}_i \cdot \vec{S}_{i+1} + J_3 \vec{S}_i \cdot \vec{S}_{i+2}$, where the NN interaction is either ferromagnetic ($J_1 > 0$) or antiferromagnetic ($J_1 < 0$) in nature and $\vec{S}_i$ is the spin in the i-th layer. This leads to a helimagnetic phase when $|J_1| < 4J_3$ which undergoes a transition to the ferromagnetic phase when $|J_1| > 4J_3$. Some experimental systems appear to conform to this picture.

5.2 Theoretical model

In order to compare the theoretical phase diagrams with the experimental ones, we make the following simplifying assumptions: The bent molecules are supposed to rotate freely and form a uniaxial SmA phase (the paraelectric phase) at high temperatures. As the medium is cooled from this uniaxial SmA phase, there can be a transition to a phase in which the bent molecules pack efficiently to produce layers with a transverse polar order. If in addition, the molecules carry a transverse component of a permanent dipole moment in the plane of the bend, such a medium will exhibit a transverse polarization. We assume that such layers with polar order arise mainly due to the *intra* layer interactions and these polarized layers are coupled *weakly* through NN and higher neighbour interactions. For the sake of simplicity we do not consider the possibility of a transition from the polarized state to a biaxial SmA phase in which the bend directions of the molecules preferably lie in a plane within the layer but there are as many molecules with the bent directions pointing 'right' as there are pointing 'left' and as such the layers are not polarized.

We can now develop a Landau theory for an N-layer system using the 2-d in-plane polarizations $\vec{P}_i = P\hat{a}_i$, $i = 1 \ldots N$ of the layers as the order parameters. As the magnitude P of $\vec{P}_i$ arises due to *intra* layer interactions, it is assumed to be independent of i. The first two terms in Eq. 5.1 (given below) take into account the transition from an unpolarized to a polarized state of the smectic layers. In addition, we have to take into account *inter* layer interactions in the theory. As in the case of straight rod-like molecules discussed in chapter 2, anisotropic dispersion interactions between the bent molecules in successive layers favour the molecules to lie in a plane giving rise to the J_2-term in **Eq.** 5.1. Further, the anisotropic dispersion interaction between the *end groups* facing each other in successive layers is lowered if they have opposite tilt (see discussion in Sec. 2.4.1). From Fig. 5.2, it can be seen that for bent molecules this favours a *ferroelectric* ordering of the

$\hat{a}_i$'s in successive layers. On the other hand, the entropy gain due to translational motion of the molecules will be maximized if the two arms facing each other of the bent molecules in successive layers have the same tilt. This favours an *antiferroelectric* ordering of the $\hat{a}_i$'s in successive layers. Therefore, the nearest neighbour interactions between the layers have competing contributions from entropy and the interaction between the molecules. This gives rise to the explicit temperature dependence of the coefficient J_1 in Eq. 5.1 for the nearest neighbour interaction between the layers. At higher temperatures entropy gain dominates favouring the antiferroelectric configuration whereas at lower temperatures the attractive interactions between the molecules dominate favouring the ferroelectric configuration. It should be noted that the bent geometry of the molecules produces a reverse preference for these interactions compared to those for tilted straight rod-like molecules considered in earlier chapters.

Further, following an argument given by Bruinsma arid Prost [21] (which is described in chapter 2), the thermal splay fluctuations of $\vec{P}$ produce charge densities which favour an antiferroelectric long range interaction between the layers. This interaction is $\propto \mathbf{P}^2/\mathbf{K}$, where $\mathbf{K}$ is a relevant curvature elastic constant, and the ratio can be expected to be independent of $\mathbf{P}$. In the following we introduce tlie next nearest neighbour '(NNN) interlayer interaction to take into account this process. In view of these arguments, we write the free energy per unit area of the N-layer system as

$$\mathcal{F}^{(\mathrm{N})} = \sum_{i=1}^{N} \left[\frac{A}{2}P^2 + \frac{B}{4}P^4 + J_1 P^2 \hat{a}_i \cdot \hat{a}_{i+1} - J_2 P^4 (\hat{a}_i \cdot \hat{a}_{i+1})^2 + J_3 \hat{a}_i \cdot \hat{a}_{i+2} \right] \tag{5.1}$$

where $A = a(T - T_{PU})$, T_{PU} being the temperature at which the sniectic layers have transition from the polarized to unpolarized state. In tlie unpolarized (paraelectric) phase the molecules freely rotate and there is no long range order of the bend directions of the molecules. This unpolarized smectic phase however may not be realized for all samples as the smectic layer order may break below T_{PU}. We assume that $J_1 = j(T - T_{AF})$, where T_{AF} is the temperature at which J_1 changes sign to favour antiferroelectric inter layer order at higher temperatures. Note that $\mathbf{P}$ does not explicitly figure in the J_3-term for reasons mentioned earlier. The ANNNXY model used for describing magnetic systems has only the J_1 and J_3 terms [39]. The J_2 term which is important in tlie present physical problem introduces new features in the phase diagram as we will discuss below.

For the calculation of the phase diagram exhibited by the model, without loosing generality, we assume that the A and B coefficients are much stronger than the interlayer J-interactions in Eq. 5.1 so that the magnitude $\mathbf{P}$ of the polarization of the layers is governed by the first two terms in Eq. 5.1. Minimizing with respect to P then gives the equilibrium polarization as

$$P^2 = \frac{\alpha(T_{PU} - T)}{B} \tag{5.2}$$

To find the different possible stable structures involving the polarized layers, we write the J-dependent part of the free energy as

$$\mathcal{F}^{(\mathrm{N})} = \sum_{i=1}^{N} \left[J_1 P^2 \cos \delta\phi_i - J_2 P^4 \cos^2 \delta\phi_i + J_3 \cos(\delta\phi_i + \delta\phi_{i+1}) \right] \tag{5.3}$$

where $\delta\phi_i$ $(= \phi_{i+1} - \phi_i)$ is the difference in azimuthal angles of $\hat{a}_{i+1}$ and $\hat{a}_i$. Since $\delta\phi_i$ are coupled only through nearest neighbours, we can use the effective potential method as described below to determine the ground state configuration of the model.

5.3   Calculations and discussion

5.3.1   Effective potential method

Let us consider the one-dimensional chiral xy model described in Sec. **3.4.2** in the presence of an external field. The Hamiltonian of the model can be rewritten as

$$H(\{\theta_n\}) = \sum_n [W(\theta_n - \theta_{n-1}) + V(\theta_n)], \tag{5.4}$$

where

$$W(x) = 1 - \cos(x - \mathbf{A}) \tag{5.5}$$

and

$$V(x) = \mathbf{E}(1 - \cos px). \tag{5.6}$$

Here θ_n is the angle between the spin vector at the nth site arid the applied field, Δ is the chirality parameter and E is the magnitude of the field. In spite of the apparent simplicity of the model, finding the ground state configurations of the spins in the presence of field is quite formidable. The complexity arises mainly from two sources, *viz* the non-convexity of the interaction potential $W(x)$ and the presence of many local minima of the Hamiltonian. To circumvent these two problems Chou *et al.* [47] developed the so called *effective* potential method to find the ground state of the model numerically. Though for the description of the method we have chosen 1-d chiral xy model, the approach is quite general and can be applicable to other systems with nearest neighbour interactions. In the following we will closely follow the description given by Yokoi et al. [22] for the method. For a more detailed discussion, we refer to the original paper of Chou et nl. [47].

Consider one of the spins in the chain when the system is in its ground state. When we rotate this spin and let all other spins rearrange to minimize the total system energy, the final state will, in general, have higher energy than the ground state. This energy is expected to be finite as it has created a local excitation or defect in the chain. One can think of this excess energy as an effective potential felt by the spin due to all other spins in the chain. Thus we define formally the "left effective potential" acting on the nth spin by the expression

$$R(\theta_n) = min \left\{ \sum_{i \leq n} [W(\theta_i - \theta_{i-1}) + V(\theta_i) - \lambda] \right\}, \tag{5.7}$$

where λ is the ground state energy per spin and the minimum is to be taken over the spin angular variable θ_i for $i \leq$ n. Analogously, the "right effective potential" acting on the nth spin is defined as

$$S(\theta_n) = min \left\{ \sum_{i \geq n} [W(\theta_i - \theta_{i-1}) + V(\theta_i) - \lambda] \right\}, \tag{5.8}$$

where the minimum is to be taken over the variables θ_i for $i \geq n$. The total effective potential for a spin in the chain due to all other spins is then given by

$$F(\theta) = R(\theta) + S(\theta) - V(\theta), \tag{5.9}$$

where the potential V(0) has been subtracted to avoid counting it twice. If $V(\theta)$ is symmetric *i.e.*, $V(\theta) = V(-\theta)$, comparison of Eq. 5.7 and 5.8 gives

$$S(\theta) = R(-\theta) \tag{5.10}$$

and in this case determination of $R(\theta)$ is enough to describe the system.

As shown by Chou *et al.* [47], the real utility of the method lies in the fact that the left effective potential obeys a minimization eigen value equation

$$\lambda + R(\theta') = V(\theta') + min_\theta[W(\theta' - \theta) + R(\theta)] \equiv \mathcal{K}R(\theta'). \tag{5.11}$$

Eq. 5.11 defines a map $0 \to \tau(\theta)$, where $\tau(\theta)$ is the set of points where the minimum of the right hand side occurs. Starting from an arbitrary initial point θ_o, we can generate an infinite sequence $\{\theta_i\}_{i<0}$, where

$$\theta_{i-1} \in \tau(\theta_i). \tag{5.12}$$

Physically we expect that after an initial transient behaviour representing the relaxation of the spins, the orbit will tend to an attractor corresponding to a possible ground state of the system. Similarly, a minimization eigen value equation for the right effective potential S defines another one dimensional map $\theta \to \sigma(\theta)$, which by iteration also leads to a possible ground state of the system.

Thus the problem reduces to solving the minimization eigen value equation (Eq. 5.11) for R and A. Eq. 5.11 can be solved numerically by an iterative procedure in which 0 varying between 0 and 2π is discretized in ν equal intervals. The straightforward iterative scheme suggested by Eq. 5.11

$$R^{j+1}(\theta) = \mathcal{K}R^j(\theta) - \lambda^j, \tag{5.13}$$

where λ^j is such that

$$min_\theta[\mathcal{K}R^{j+1}(\theta)] = 0, \tag{5.14}$$

has some convergence problems [47]. Therefore, an alternative scheme that seems to converge in general has been proposed which takes the average of two previous R as

$$R^{j+1}(\theta) = \frac{1}{2}[\mathcal{K}R^j(\theta) + R^j(\theta)] - \lambda^j, \tag{5.15}$$

where λ^j is defined according to Eq. 5.14. The choice of initial R function seems to be unimportant. For example one can start with $R^0 = V$. The recursion relation Eq. 5.15 is iterated until self consistency is achieved, that is, until

$$max_\theta[|R^{j+1}(\theta) - R^j(\theta)|] < \epsilon, \tag{5.16}$$

where $\epsilon \approx 10^{-8}$. Then λ^j is the approximation for the ground state energy per spin A. The ground state spin configuration is obtained by iterating the τ-map discarding the initial transient behaviour.

The main drawbacks of this method are: (a) due to the discretization of the angular variable θ into finite number of intervals, the ground state configurations obtained numerically are always commensurate. (b) The method is developed taking only nearest neighbour interactions. A straightforward generalization to include the next nearest neighbour interactions is again computationally costly.

However, coming back to our problem, as mentioned in Sec. 5.2, it is clear from Eq. 5.3 that in the absence of field $\delta\phi_i$ are coupled only through nearest neighbours. Thus we can apply the effective potential method described above to construct the ground state phase diagram predicted by the model.

5.3.2   Theoretical phase diagrams

Clearly when $|J_1 P^2|$ is sufficiently large, either ferroelectric $(\delta\phi_i = 0, J_1 < 0)$ or antiferroelectric $(\delta\phi_i = \pi, J_1 > 0)$ structures are stabilized. The only other possible ground states have either a *uniform* helical structure with $\cos\delta\phi = J_1 P^2 / 2(J_2 P^4 - 2J_3)$ or a *non-uniform* (2,2) anti-phase structure in which 4 layers with $\delta\phi_i = 0$ and $\delta\phi_{i+1} = \pi$ form the repeating unit. When $J_2 P^4 < J_3$, as $|J_1 P^2|$ is decreased, a helical structure which breaks the chiral symmetry of the medium is stabilized. This is reminiscent of the helimagnetic phase found in magnetic systems [39]. The helical structure is clearly a consequence of the competition between J_1 and J_3 interactions. As the helical symmetry is broken spontaneously, both right handed and left handed structures are equally probable.

Detailed calculations have been made for $a = 0.088$, $T_{PF} = 187.0°C$, $B = 13.8$, $j = 2.178$ x 10^{-4}, $T_{AF} = 175.0°C$ and different values of J_2 and J_3. The temperature-J_2 phase diagram for $J_3 = 4.0$ x 10^{-5} is shown in Fig. 5.3a. As $J_1 P^2$ is rather small and positive just below T_{PU}, the paraelectric phase has a second order transition to a helical phase H_{af} in which $\delta\phi_i$ varies from $\pi/2$ to π as the temperature is lowered. At lower temperatures P^2 grows and when

$$|J_1|P^2 = 2(2J_3 - J_2 P^4) \tag{5.17}$$

is satisfied, the helielectric phase undergoes a second order transition to the antiferroelectric (AF : ↑↓ $\cdots$) phase. As the temperature is lowered in this phase, $J_1 = j(T - T_{AF})$ decreases and Eq. 5.17 is again satisfied so that the medium reenters the helical H_{af} phase. As $|J_1|$ decreases further, the free energy given by Eq. 5.3 exhibits another minimum for a 4-layer anti-phase structure with $\delta\phi_i = 0$ and $\delta\phi_{i+1} = \pi$ ((2,2)AP : ↑↑↓↓ $\cdots$). As the temperature is lowered below T_{AF} and the magnitude of negative J_1 grows, we get a first order transition to the helical H_f phase with $\delta\phi_i < \pi/2$. Equating the free energy per layer in these helical and the (2,2)AP phases, the boundary describing the first order transition between them satisfies

$$J_1^2 = 4J_2(2J_3 - J_2 P^4) \tag{5.18}$$

Note that when $J_2 = 0$ the (2,2)AP structure is degenerate with the helical one with $\delta\phi_i = \pi/2$. At an even lower temperature, when Eq. 5.17 with negative J_1 is satisfied, we get the uniform ferroelectric (F : ↑↑ $\cdots$) phase. It should be mentioned here that for reasons described earlier, the temperature sequence of occurrence of the F and AF phases is reversed in the present case compared to that in the AFLC made of straight rod-like molecules discussed in earlier chapters. As J_2 is increased the second order phase
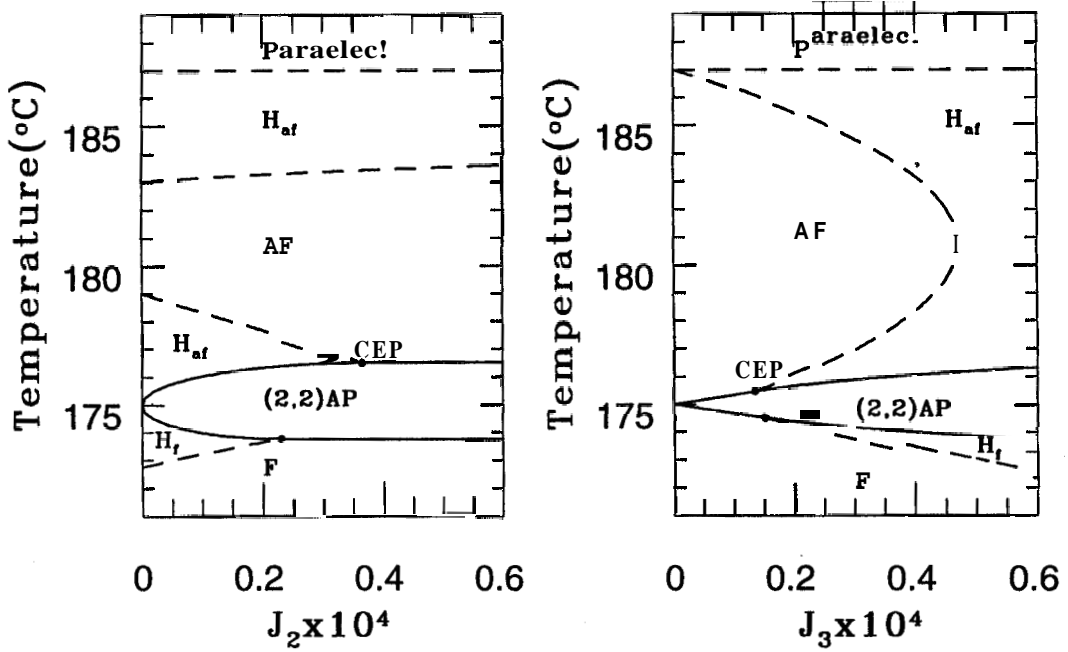
Fig. 5.3: (a) Temperature-J_2 phase diagram. Dashed lines indicate second order transitions and full lines first order transitions. CEP represents critical end point (b) Temperature-J_3 phase diagram.

boundary between the lower temperature helical phases and the F or AF phases meet the first order line involving the (2,2)AP structure at *critical **end** points* (CEP). Beyond the corresponding J_2 values, the helical phase is not stable, and the (2,2)AP has direct first order transition into AF and F phases. Again equating the free energy per layer, the first order phase boundary between AF and (2,2)AP phase satisfies

$$J_1 P^2 = 2J_3. \tag{5.19}$$

The phase boundary corresponding to F and (2,2)AP phase can be obtained from Eq. 5.19 by replacing J_1 by $-J_1$. Indeed for large values of $J_2 P^4$, the molecules prefer to lie in the same plane and the structures correspond to those given by the Ising model and the phase diagrams predicted by the ANNNI model [39] becomes relevant. We believe that this regime may not be relevant to liquid crystals.

The temperature$-J_3$ phase diagram is shown in Fig. 5.3b for $J_2 = 1.0 \times 10^{-5}$ cgs unit brings out the fact that the helical phase owes its origin to the J_3-interaction. As J_3 is increased, the range of the higher temperature heliphase H_{af} increases and further, the (2,2)AP phase intervenes between the AF and F phases. At higher values of J_3, the H_{af} phase reenters between the AF and (2,2)AP phases and the H_f phase is inserted between the (2,2)AP and F phases. As J_3 is increased further, the temperature range of AF phase decreases and finally disappears so that the medium exhibits only an H_{af} phase which directly goes to the (2,2)AP phase. The equations of the phase boundaries corresponding to the transition between the respective phases are again given by Eq. 5.17, 5.18 and 5.19. Note that at the point $J_1 = 0$ (at $T = 175°C$) and $J_3 = 0$, the model exhibits an infinite degeneracy with respect to the structures consisting of any sequence of polarization of the layers all lying in the same plane.

5.3.3   comparison with experiments

Recently achiral compounds with strongly bent molecules have been synthesized [25] and found to exhibit transverse polarization. The molecular structure of the compound 2_8 with an octyloxy end group is shown in Fig. 5.1. More recently, analogous 1, compounds with alkyl instead of alkoxy end groups have been synthesized [26]. The preliminary physical studies show several interesting features. Polarization measurements have been made on the compound 2_8, while x-ray measurements have been made on the compound 1_8. We quote the relevant results on these compounds. Both have a transition from the isotropic phase to a SmX_1 phase which is *helical* in nature. 2_8 exhibits a strong transverse polarization of ~ 60 nC/cm^2 in this phase. Both undergo a transition to a SmX_2 phase at a lower temperature, which is not *helical* and the 2_8 compound does not have any polarization in this phase. However, x-ray studies on the 1_8 compound shows a $10\mathring{A}$ increase in layer spacing between SmX_1 and SmX_2 phases which the authors have interpreted to mean a change in conformation of the molecules such that the bend angle decreases in the SmX_2 phase. Interestingly, the compound 1_8 also exhibits a transition to a SmX_3 phase which has the same layer spacing as SmX_2 but is helical in nature. The authors have stated that the helical structures may arise from conformational chirality and/or flexoelectric effect.

We feel that the observations can be accounted for by the ANNNXY model presented above. We can identify the SmX_1 phase with the H_f phase. When the molecular

conformation changes at a lower temperature, we can expect that both the magnitudes of the negative J_1 parameter as well as J_2 *decrease* due to the smaller bend angle and larger interlayer separation. This should mean that for example T_{AF} itself changes for the new conformation. For the present purpose, we can assume that the medium is now characterized by a smaller negative value of J_1 which takes it to the $(2,2)\mathrm{AP}$ phase which does not have a net polarization or helicity (as in $\mathrm{SmX_2}$ phase). As the medium with the molecules in the new conformation is cooled, it again reenters the H_f phase (as in $\mathrm{SmX_3}$ phase) due to temperature effects alone as seen in fig. 5.3. Interestingly, in the compounds synthesized upto now, the helielectric $(\mathrm{SmX_1})$ phase directly undergoes a transition to the isotropic phase. Very recent experiments have shown that these compounds exhibit both left handed and right handed helices as expected from the spontaneous breaking of chiral symmetry [61]

5.4   Conclusion

We have proposed an ANNNXY model for polar biaxial smectic liquid crystals with nonchiral but bent molecules which may exhibit transverse polarization. In comparison with the magnetic case, we have to include an additional term depending on $\cos^2 \delta\phi_i$, which changes the phase diagram compared to the magnetic case. In particular helielectric phases as well as $(2,2)$ anti-phase structures are predicted in appropriate range of parameters in addition to the usual ferroelectric and antiferroelectric phases. Interestingly very recent experimental studies have shown that such systems exhibit helielectric as well as antiferroelectric phases which may be tentatively identified with the predicted phases. However, an unambiguous identification requires further experimental studies on the structures exhibited by these novel compounds.

Chapter 6

Electrooptic studies on AFLC

6.1 Introduction

In the antiferroelectric liquid crystalline phase, chiral molecules tilt essentially in opposite directions in successive layers, leading to a net cancelation of the polarization in the medium [2, 3, 15, 62]. However, by applying a sufficiently strong electric field, it is possible to get an antiferroelectric to ferroelectric transition and a trilevel switching which is being explored for exploitation in display devices. As described in' previous chapters, many compounds which exhibit the antiferroelectric SmC_A^* phase often exhibit a sequence of other liquid crystalline phases. The prototype compound MHPOBC for example exhibits on cooling the sequence: SmA- SmC_α^*- SmC_β^*- SmC_γ^*- SmC_A^*- SmI_A^*- cryst..

Dielectric measurements have been extensively used to study the phase transitions in these compounds [63, 64, 65]. In the paraelectric SmA phase, the dielectric response has a contribution from the director tilt fluctuations or the **soft** mode. On approaching the SmA to SmC^* transition, the soft mode dielectric strength diverges and its relaxation frequency exhibits a critical slowing down. The spontaneous polarization gives rise to a large contribution to the dielectric response in the ferroelectric SmC_β^* phase. In this phase, besides the soft mode, the dielectric response has contribution from another mode due to the phase fluctuations of the director or the so called Goldstone mode. The Goldstone mode is characterized by a relaxation frequency which is usually less than 1 kHz for most of the compounds. Because of the much stronger contribution from the Goldstone mode, at low frequencies the soft mode contribution to the dielectric constant can be measured easily only near the SmA to SmC_β^* transition point [66] or by quenching the Goldstone mode by applying a dc bias field. The net polarization in the ferrielectric (SmC_γ^*) phase is reduced giving rise to a relatively lower dielectric response. In the antiferroelectric phase, the net polarization is essentially zero and the dielectric response in this phase is even lower compared to the ferrielectric phase. The dielectric spectrum in the antiferroelectric SmC_A^* phase exhibits two absorption peaks observed in the kHz and MHz range respectively. It has also been reported [67] that by applying a bias field a third absorption peak can be resolved in the dielectric spectrum of the SmC_A^* phase. The actual modes corresponding to these relaxation processes are not very clear from the literature. The third process observed in the presence of a bias electric field has been attributed to an 'induced Goldstone mode'. The high frequency relaxation process in the absence of the bias field has been interpreted

by Moritake *et al.* [67] as a soft mode, while Hiraoka *et al.* [68] have attributed this process to an anti-phase Goldstone mode. Further, the low frequency mode is assigned by Moritake *et al.* [67] and Hiraoka *et al.* [68] to a 'non-collective' molecular reorientation around the short axis, a process which is usually observed in the quasi homeotropic orientation of tilted smectics. On the other hand this is attributed to an in-phase Goldstone mode by Buivydas *et al.* [64].

The electroclinic effect in which an external field induces a tilt in the SmA phase has been a very useful method of exploring the critical soft mode in the SmA phase close to the SmA-SmC^* transition point [69]. The electrooptic response in the lower temperature tilted phases can also be expected to yield very useful information about the structures and dynamics in these phases. Indeed there have been many electrooptic measurements on compounds exhibiting antiferroelectric phases [70, 71, 72, 73]. However, when we undertook the electrooptic measurements, there were only a couple of measurements [72, 73] made on relatively thick ($\sim 20\mu$m) samples in which the electrooptic signal was hardly detected in the antiferroelectric phase.

We conducted electrooptic measurements on two compounds exhibiting the sequence SmA–SmC^*_α–SmC^*_β –SmC^*_γ–SmC^*_A–SmI^*_A on *cooling* using relatively *thin* samples (2 to 5 pm). We found that we could detect the phase transitions quite clearly using such samples. Indeed in well aligned samples, we could not only get a reasonable electrooptic signal in the antiferroeletric phase, but detect the antiferroelectric to SmI^*_A transition as well. Moreover the electrooptic response shows a double relaxation process in the ferrielectric, antiferroelectric as well as in the SmI^*_A phases. We attribute the mode with the higher relaxation frequency in the antiferroelectric phase to a soft mode in which molecules in neighbouring layers tilt asymmetrically under the action of the external field.

6.2   Experimental

6.2.1   Electrooptic measurement setup

The block diagram of the experimental setup for studying the electrooptic response is shown in Fig. 6.1. A He-Ne laser is used as the light source. The light beam from the laser falls on a beam splitter (BS). The reflected component of the laser beam from BS is monitored using a photo-diode amplifier assembly (PD_1) model OSI-5K. The output voltage from PD_1 is measured using one of the channels in the rear panel of the digital multimeter (DMM) model HP 57A. This reference photo-diode allows us to take into account the intensity fluctuations of the incident laser beam. The transmitted part of the laser beam from BS, after passing through the polarizer (P) is incident on the sample. The sample is kept in an INSTEC HS1-i hot-stage mounted on the microscope table. The transmitted light from the sample, after passing through the analyzer (A) is monitored using a PIN photo-diode. The output from the PIN photo-diode is amplified using an OPAMP in the *trans impedance* mode *i.e.,* it acts as a current to voltage converter. The circuit diagram of this amplifier is shown in Fig. 6.2. The amplifier circuit is placed close the PIN photo-diode and shielded to reduce pick up of noise. This PIN photo-diode and amplifier assembly is denoted as PD_2 in Fig. 6.1. The output from PD2 is connected to another channel in the rear panel of DMM to measure the dc component of the optical
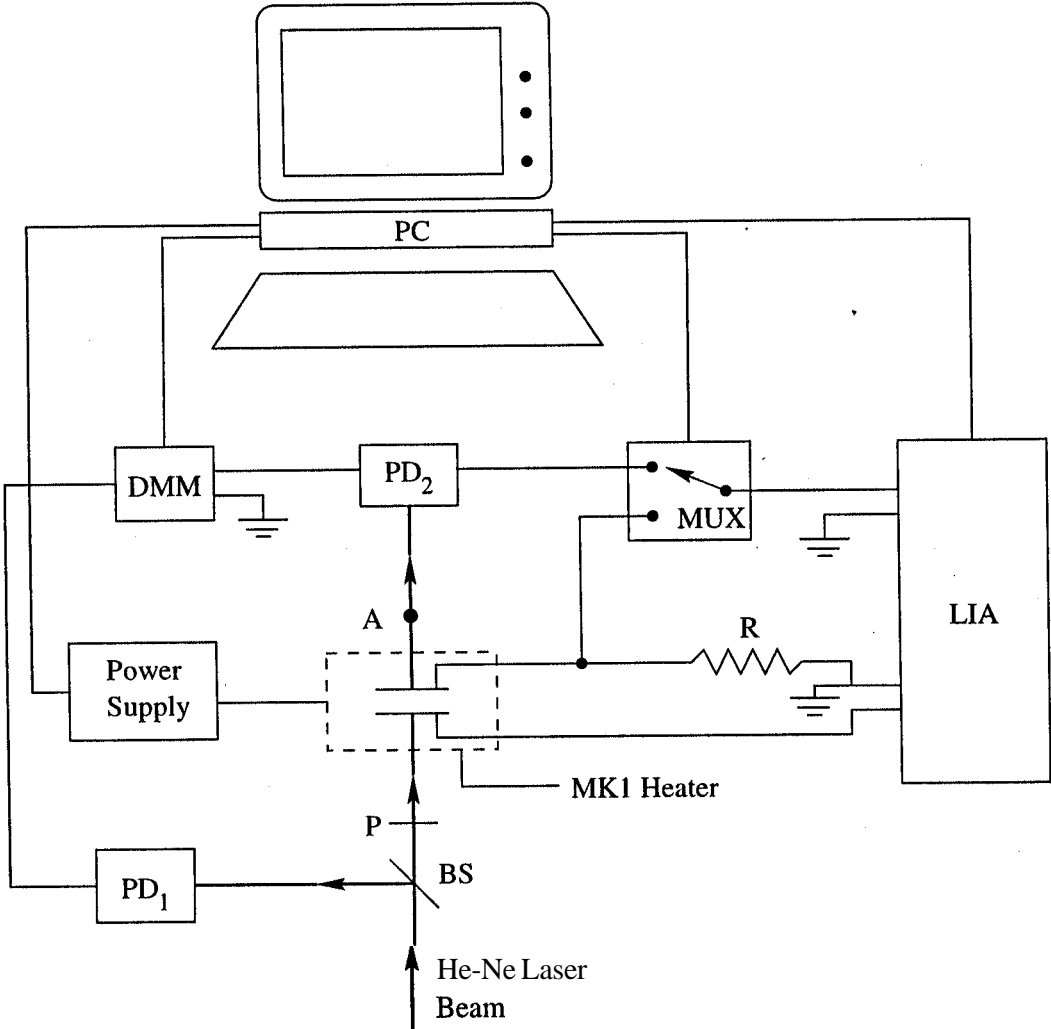
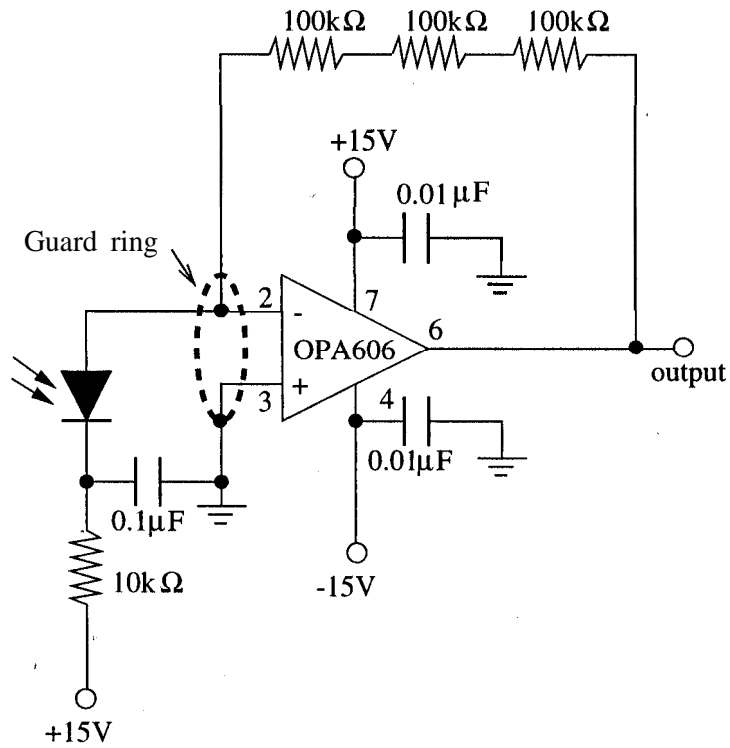Fig. 6.1: The block diagram of the electrooptic measurement setup.

Fig. 6.2: The amplifier circuit in the trans-impedance mode to convert the photo-diode current to voltage.

signal. The output from PD_2 is also connected to the input of a lock-in amplifier (LIA), model PAR 5302, through the multiplexer (MUX) for measuring the ac component of the optical signal. The sinusoidal output voltage from the builtin oscillator of the LIA is applied to the sample cell through a resistance R connected in series with the sample cell. The conductivity signal through the cell can also be measured by measuring the voltage drop across R. For simultaneous measurements of the optical and the conductivity signals, both these signals are fed to the LIA input via a multiplexer (MUX), which can be programmed to switch between these two measurement modes. However, we will not show the conductivity measurements in the following.

The temperature of the sample is controlled using an INSTEC HS1-i hot-stage and a plug-in computer card (MK1) which can be fitted in one of the extension slots of a computer. As the thermistor built in the hot-stage to measure the temperature is not very close to the sample, we have mounted another RTD near the sample to realize better measurement of the temperature of the sample. The RTD has been calibrated in the temperature range $(30\text{-}250°\text{ C})$ of our interest and the temperature is measured in terms of the resistance of the RTD. The resistance of the RTD is measured usipg the front panel connection of the DMM. A wooden box with thermocol lining has been built around the microscope to enhance the temperature stability. The dc power supply (APLAB 5376) used for temperature control in our experiments is found to have reasonable stability. The temperature stability obtained in our setup is better than 5 mK.

The temperature control as well as the measurement are automated by interfacing the programmable instruments to an IBM PC through a GPIB card (model KEITHLEY). The interfacing has been done using C++ language. The C++ language has been chosen as it provides more flexible and easily reusable code through its object oriented concepts. The programs written for this purpose have the following options:

Temperature Run: In this option, the measurements are carried out as a function of temperature but at a predefined fixed frequency of the applied voltage. The temperature variation can be heating, cooling or both. The program automatically adjusts the temperature step as well as the amplitude of the applied voltage during the run to ensure that the phase transition points are not missed and the response of the system is within two specified limits. Also the user can choose the fundamental or higher harmonics of the signal to be measured. This option is used to quickly detect the transitions between the various phases exhibited by antiferroelectric liquid crystals.

Frequency Run: In this more general option the electrooptic response of the sample is measured by varying both temperature and frequency. This option has all the facilities of the temperature'run mentioned above except the temperature step in this option is not variable.

6.2.2   Samples used in the experiments

The molecular structures of the compounds used in the experiments are shown in Fig. 6.3. The compounds exhibit the following sequence of phases:
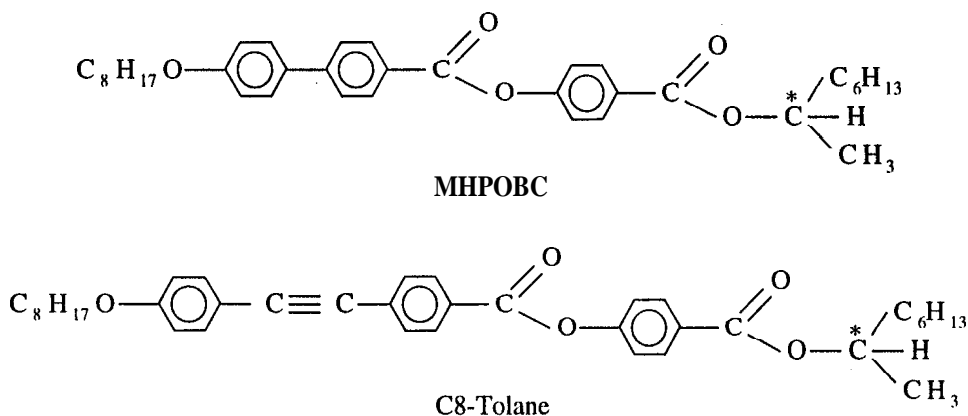
$C_8H_{17}O$ —⬡—⬡— C(=O) — O —⬡— C(=O) — O — $\overset{*}{C}$—H — C_6H_{13}, CH_3

MHPOBC

$C_8H_{17}O$ —⬡— C≡C —⬡— C(=O) — O —⬡— C(=O) — O — $\overset{*}{C}$—H — C_6H_{13}, CH_3

C8-Tolane

Fig. **6.3:** The structural formulae of the compounds used in the experiments.

1) **MHPOBC:** Crystal – 30° C – SmI_A^* – 66° C – SmC_A^* – 118.3° C – SmC_γ^* – 119° C – SmC_β^* – **120.7"** C – SmC_α^* – 122° C – SmA – 156° C – Isotropic.

2) **C8-tolane:** Crystal – 67.6° C – SmI^* – 71.6° C – SmC_A^* – **95.1"** C – SmC_γ^* – **97"** C – SmC_β^* – 104° C – SmC_α^* – 105.5° C – SmA – 135° C – Isotropic.

Both the samples were synthesized at Centre de Recherche Paul Pascal (CRPP) Bordeaux, and the transition points correspond to the data from DSC measurements.

6.2.3 Sample cell preparation

In our electrooptic measurements, we have studied the response in two different geometries of the sample *viz.* the *homogeneous* and *homeotropic* geometries. We briefly describe below these two .geometries of the sample and the preparation of the sample cells to achieve the same.

Homogeneous alignment

In this geometry the alignment of the nematic director $\hat{n}$ at the glass plate is parallel to the plate as well as to an imposed preferred direction as shown in Fig. 6.4a. To obtain such an alignment of the sample, the glass plate has to be coated with a thin layer of *polyimide* and then the plate is cured at 200° C for an hour. The glass plate is then rubbed unidirectionally to provide the preferred direction of alignment of the director $\hat{n}$ at the plate. In order to facilitate the application of .an electric field the glass plates used are indium tin oxide (ITO) coated. The ITO coating acts as a thin transparent electrically conducting electrode, making it possible to conduct electrooptical measurements. A sample cell within which the nematic director $\hat{n}$ is parallel to the bounding glass plates and unidirectionally oriented can be obtained as follows. Two such rubbed polyimide coated plates are sandwiched together leaving a small gap between them by using mylar spacers. The plates are placed in such a way that their rubbing directions are parallel to each other. The plates are usually fixed by using a high temperature glue (EPOXY).
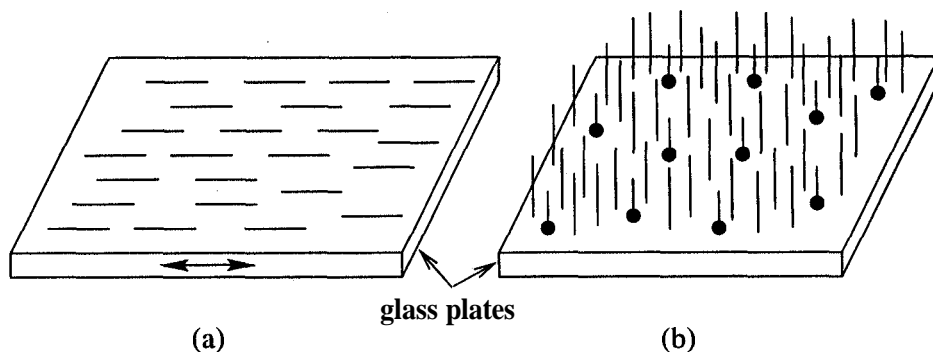
glass plates
(a)   (b)

Fig. 6.4: The alignment geometry of the liquid crystalline molecules at the glass plate. (a) Homogeneous alignment in which the molecules are parallel to the glass plate. The double arrow indicates the rubbing direction. (b) Homeotropic alignment. The molecules with solid circles at the tip represent the ODSE molecules.

By using different thicknesses of the mylar spacer, the cell thickness can be adjusted to the required value. The sample thickness used in our experiments vary between 2 to 25 μm. The sample cell thickness was measured using an interferometric technique in which white light and a constant deviation spectroscope (Adam and Hilger Ltd.) were used. The sample is filled in the isotropic phase by capillary action. Care is taken to ensure that air bubbles do not get trapped inside the sample. Generally good alignment can be obtained by slowly cooling (at the rate of 0.05" C/min) the sample to the SmA phase under a low frequency electric field.

Homeotropic alignment

In this geometry the alignment of the director $\hat{n}$ at the glass plate is perpendicular to the plate (see Fig. 6.4b). To enforce such an alignment, the glass plate is usually treated with *octadecyl triethoxy silane* or ODSE cured at 150° C for an hour. The ODSE molecules lie on the glass plate with their polar heads attached to the plate but the long aliphatic chains stick out of the plate. This provides the boundary condition to the liquid crystalline molecules with long alkyl chains to align perpendicular to the plate as shown in Fig. 6.4b. Preparation of the sample cell in this case is similar to the homogeneous case as described above. Thus in such a sample cell the director A is uniformly oriented and is perpendicular to the plates.

The homeotropic alignment of the director $\hat{n}$ forces the layers in the smectic phase to be parallel to the glass plates. In our experiments in this geometry, we need to apply a transverse electric field parallel to the smectic layers in the various phases exhibited by AFLC. We use for this purpose two flat steel wires placed parallel to each other between the glass plates instead of the mylar spacer. As the thickness of these available wires are relatively large, the sample cells are relatively thick in this geometry. The separation between these electrodes has to be adjusted to be as small as possible to enable the application of a high field across the sample. The separation between the electrodes in our experiments varies between 50 to 200 μm.

6.3 Results and discussion

6.3.1 Homogeneous geometry

The transmitted light intensity **I** through an uniaxial sample cell of thickness d placed between crossed polarizers is given by

$$I = I_o \sin^2(2\psi) \sin^2(\frac{n \cdot \Delta nd}{\lambda}) \qquad (6.1)$$

where ψ is the angle between the optic axis and one of the polarizer directions. An is the effective birefringence of the medium. λ and I, are respectively the wavelength and the intensity of the incident light beam. In the SmA phase, the optic axis of the medium is along the director $\hat{n}$ (*i.e.,* along the layer normal). Thus from Eq. 6.1, for the bookshelf geometry of the SmA phase, the transmitted intensity is maximum when the layer normal (optic axis) is at an angle $\psi = 45°$ with respect to one of the polarizer directions. Because of the electroclinic effect, the induced tilt angle $\Delta\theta$ in the SmA phase oscillates at the frequency of the applied ac electric field. In the bookshelf geometry of the SmA phase this causes a small change $\Delta\psi = \Delta\theta$ in the azimuthal direction of the optic axis. Then the corresponding change in the transmitted intensity is given by

$$\Delta I = [2I_o \sin^2(\frac{\pi \Delta nd}{\lambda}) \sin 4\psi] \Delta\psi \qquad (6.2)$$

From Eq. 6.2, it is clearly seen that the maximum in ΔI occurs at $\psi = \pi/8$. Thus in all our electrooptic measurements in the homogeneous geometry, the cell is placed in such a way that the director $\hat{n}$ in the SmA phase makes an angle $\pi/8$ with respect to the polarizer. In this setting, the electrooptic signal in the SmA phase between crossed polarizers has maximum electroclinic f-response.

The temperature-runs were taken at relatively low frequencies such that the electrooptic response has contributions from the Goldstone as well as the soft mode. These runs were generally used to detect the transitions. The applied voltage was controlled to get a more or less constant optical signal. This ensures that we are generally in the *linear regime.* Thus, the applied voltage is $\sim$0.6 V/μm far above SmC$_\alpha^*$ to SmA transition point and comes down to $\sim$15 mV/μm near SmC$_\alpha^*$ - SmC$_\beta^*$ transition point and increases again to $\sim$0.6 V/μm in the antiferroelectric and SmI$_A^*$ phases. The measured amplitude of the electrooptic response at the frequency of applied ac field (f-response) shown in the figures is normalized as [f-response/(electric field x dc-response)], which makes the f-response independent of the incident laser intensity and the cell thickness. In the following we will call this normalized electrooptic f-response as f-signal for the sake of simplicity.

The temperature dependence of the f-signal of a 4.3 μm sample of MHPOBC in the cooling mode is shown in Fig. 6.5 at a frequency of 752 Hz. The peak at the highest temperature corresponds to the SmA-SmC$_\alpha^*$ phase transition. Previous experiments [74] show that the pitch in MHPOBC is usually ≥ 1 μm and changes sign across the SmC$_\beta^*$ to SmC$_\gamma^*$ transition. It is also found to diverge in the antiferroelectric phase. Hence our sample which is $\simeq 4.3$ μm thick can be expected to be in an *unwound* state at least in the antiferroelectric range [75]. The highest peak presumably corresponds to SmC$_\alpha^*$ to SmC$_\beta^*$ transition. Our results can be compared with the earlier measurements by Glogarova et *al.*
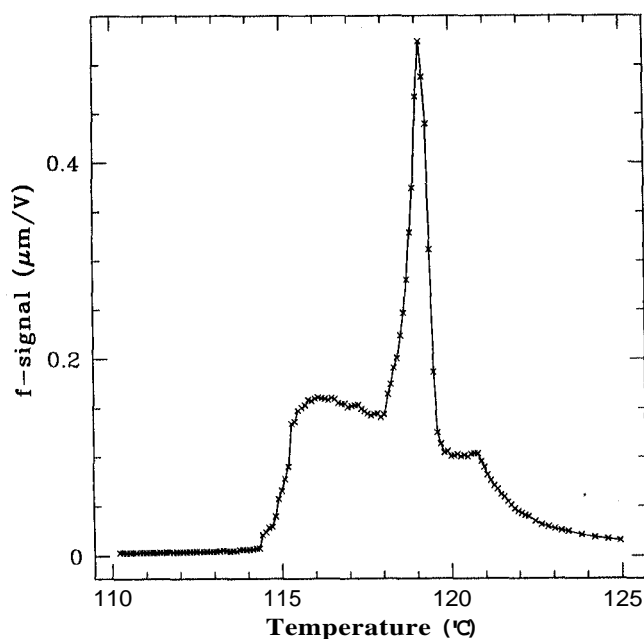
Fig. 6.5: Temperature dependence of the normalized electrooptic f-response of a **4.3** μm thick cell of the compound MHPOBC at 752 Hz in the cooling mode.

[72] on MHPOBC studied using 25 to 50 μm thick samples. The transition from SmA to SmC_α^* and SmC_α^* to SmC_β^* were marked only by changes in slope in their experiments.

We also measured the frequency dependence of the electrooptic response to find the relaxation frequencies (see Fig. 6.6) in the SmA, ferroelectric and ferrielectric phases. In this initial study, we fitted the data on MHPOBC only to a single Lorentzian. As we shall see later on detailed measurements on C8-tolane indicate two different relaxation processes. Unlike in the studies of Glogarova et al. [72], who found a step-wise decrease of the relaxation frequency as the temperature was lowered across the SmA, ferroelectric and ferrielectric phases, we find a more gradual decrease as the temperature is lowered in the tilted phases. Further, we found a measurable signal even in the antiferroelectric phase which showed a relaxation at relatively high frequencies (-10 KHz).

We conducted more detailed experiments on the C8-tolane compound. The temperature dependences of the f-signal at 754 Hz on **3.3** μm and 5.2 μm thick samples are shown in Fig. 6.7. The temperature variation is very similar to that on MHPOBC. The thicker sample has a sharper drop in the vicinity of ferri- to antiferroelectric transition indicating that the cell thickness has prominent influence on these transitions. We may point out that Moritake et al. [48] found a large coexistence of ferroelectric and antiferroelectric domains in thin cells with homogeneous geometry as an MHPOBC sample was cooled from the ferroelectric phase. In the **3.3** μm thick sample visual observations in the microscope indicate such a possibility even in C8-tolane compound. The transition from the antiferroelectric phase is also found to exhibit temperature hysteresis with respect to heating and cooling. The runs clearly indicate the transition from the SmA to SmC_α^* phase. As
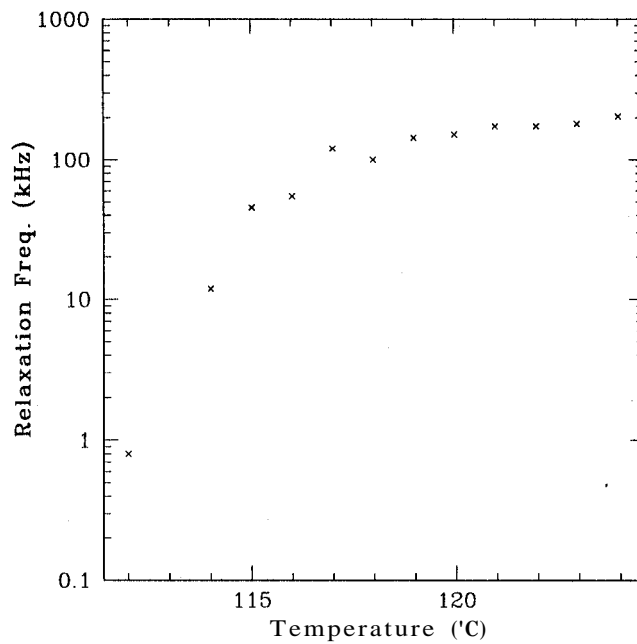
Fig. 6.6: Temperature dependence of the relaxation frequency of the electrooptic signal of MHPOBC.

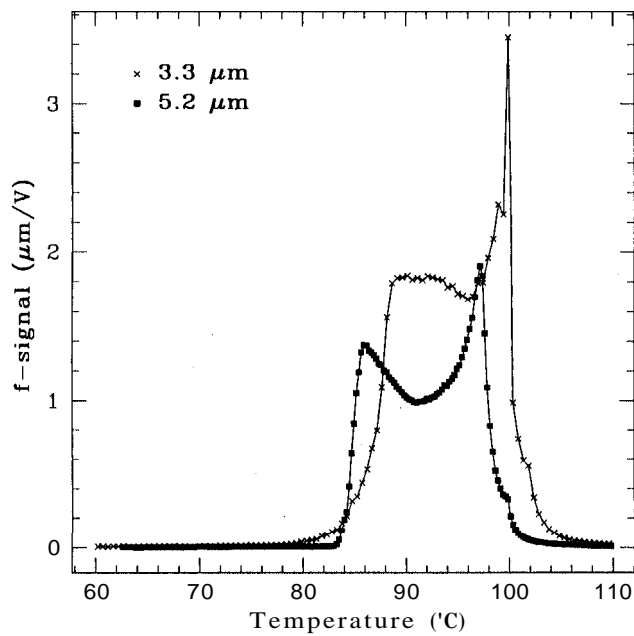Fig. 6.7: Temperature dependence of the normalized electrooptic f-signal (see text) of **3.3** μm and 5.2 μm thick sample of the C8-tolane compound at 754 Hz on cooling.
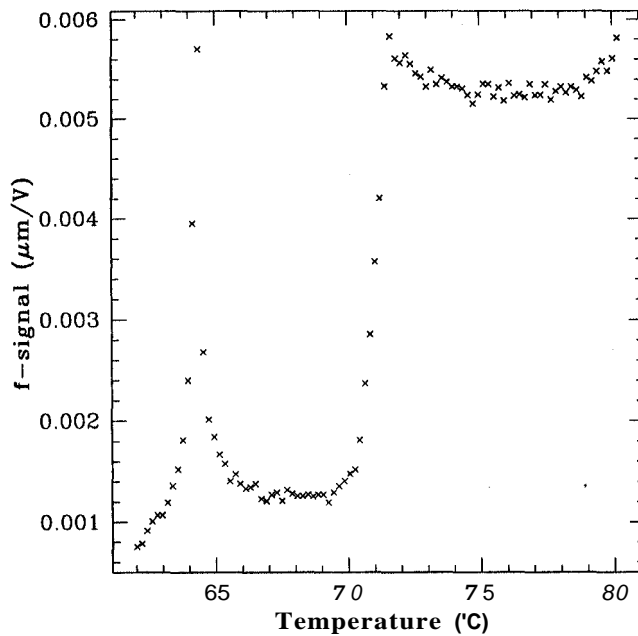
Fig. 6.8: Electrooptic signal at 754 Hz in the lower temperature range of a 2.2 μm thick C8-tolane sample showing the SmC_A^* to SmI_A^* and the SmI_A^* to crystal transitions.

---

mentioned in chapter 2, there is evidence [12, 13] from the switching current measurements that in MHPOBC the SmC_α^* phase has antiferroelectric characteristics close to the SmA to SmC_α^* transition temperature but gradually develops ferrielectric characteristics as the temperature is lowered [13]. The reduction in the electrooptic signal immediately below the SmA to SmC_α^* phase transition point and the subsequent increase at lower temperatures is consistent with the possibility that C8-tolane compound may also have a'similar behaviour. We have also studied a 2.2 μm thick sample which had an exceptionally good alignment. The electrooptic signal (Fig. 6.8) in this case was relatively high in the antiferroelectric phase and further the antiferroelectric to SmI_A^* transition at $\sim 70°$ C and the SmI_A^* to SmJ* (a 3D-crystal) transition at $\sim 64°$ C could be very clearly located. The signal drops by a large factor at the antiferroelectric to SmI_A^* transition which indicates that the hexatic SmI* phase also has an antiferroelectric order in this compound. The peak at the SmI_A^* to crystal transition probably indicates that the antiferroelectric order may be relaxed in the crystalline phase.

As the sample was heated over several days, it slowly deteriorated. It is interesting that the SmA to SmC_α^* phase transition became weaker and eventually undetectable as the deterioration worsened. Further, the temperature range over which the large drop in the f-signal across the ferro- to antiferroelectric phase occurs, appeared to widen at the expense of the antiferroelectric phase.

We have also made detailed frequency dependent measurements on the C8-tolane compound. The frequency dependences of the f-signal at different temperatures in the ferrielectric range are shown in Fig. 6.9. As is seen in Fig. 6.9, the electrooptic f-signals
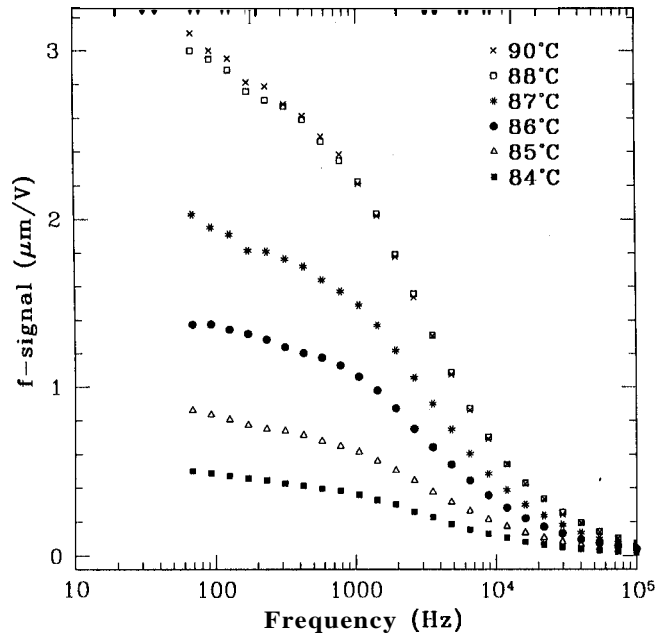
Fig. 6.9: Frequency dependences of the electrooptic response at various temperatures in the ferrielectric range.

at different temperatures in the ferrielectric range drop rapidly with increasing frequency indicating relatively low relaxation frequencies. As the temperature is lowered in the antiferroelectric phase (Fig. 6.10), the signal level gradually decreases, but more interestingly, there appear to be two relaxation processes. The frequency dependences of the f-signal in the lowest temperature ranges of the antiferroelectric phase and the SmI_A^* phase are shown in Fig. 6.11. In the SmI_A^* phase (Fig. 6.11), the signal decreases further compared to that in the antiferroelectric phase (see Fig. 6.8) and the relaxation frequency appears to shift towards lower frequencies. At the highest frequencies, we had to apply $\sim$3 V/μm to get a measurable signal in the SmI_A^* phase. We have confirmed that even in the 5.2 μm sample the electrooptic signal has a relaxation at frequencies comparable to those in the thinner samples at similar temperatures in the antiferroelectric range. However, the electrooptic response is roughly half that of **3.3** μm sample. The two relaxation frequencies were obtained by fitting the experimental data to a double Lorentzian. The relaxation frequencies for the two modes as functions of temperature are shown in Fig. 6.12. We found two relaxation processes in the ferrielectric, antiferroelectric as well as in SmI_A^* phase. From Fig. 6.12, we see that in the ferrielectric and SmI_A^* phases, the two relaxation frequencies are relatively small compared to those in the antiferroelectric phase. In the ferrielectric phase, the two relaxation frequencies remain almost constant with decreasing temperature but have jumps in both of them at the transition to the antiferroelectric phase. In our temperature runs (see Fig. 6.7) the electrooptic response has a relatively smooth variation which does not clearly indicate the transition from the ferrielectric to the antiferroelectric phase. The temperature variation of the relaxation frequencies can be used to clearly
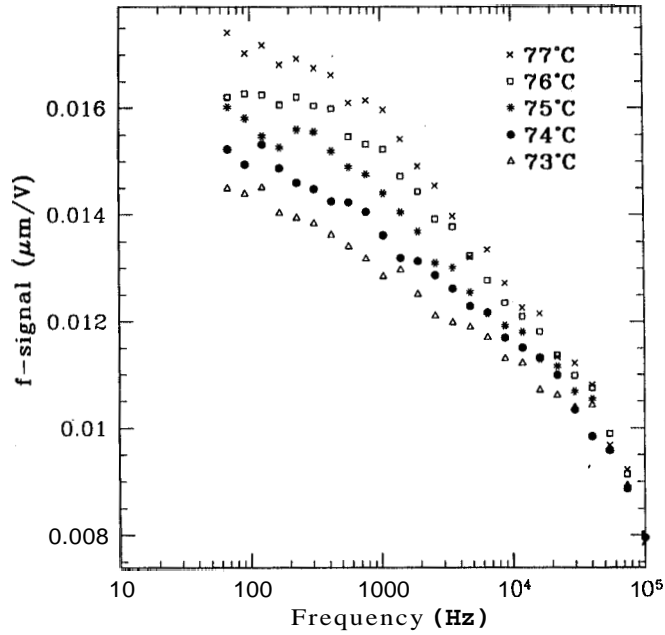
Fig. 6.10: Frequency dependences of the electrooptic response at various temperatures of the SmC_A^* phase. (note the difference in scale compared to that in Fig. 6.9).
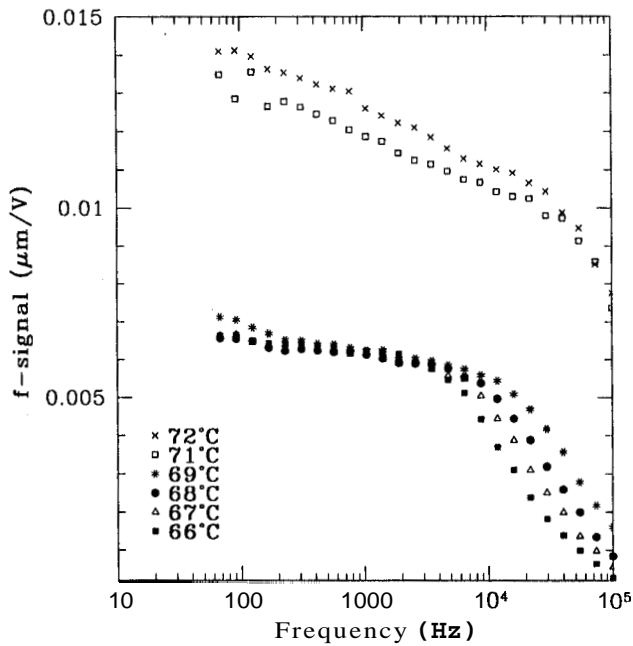

Fig. 6.11: Frequency dependences of the electrooptic signal in the SmC_A^* and the SmI_A^* phases. Note the relaxation at high frequencies.
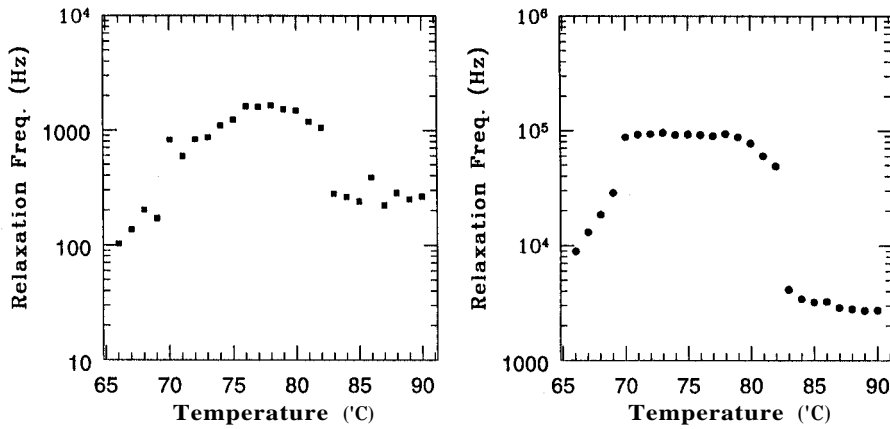
Fig. **6.12:** The double relaxation frequencies obtained by fitting the data to double Lorentzian for **3.3** μm thick c8-tolane sample.

detect the transition at about **83"** C for the **3.3** μm cell. In the antiferroelectric phase the lower relaxation frequency (< **2** kHz) shows a non-monotonic behaviour: it first increases with decreasing temperature and then decreases showing a broad peak .at about **77"** C. Our lock-in amplifier could be used only upto **100** kHz and as such the 'constant' relaxation frequency of ▪ **90** kHz seen in the antiferroelectric range is an artificial result. In the SmI_A^* phase both the relaxation frequencies are relatively low and both of them decrease as the temperature is decreased. In the lower temperature ranges of the SmI_A^* phase only the high frequency relaxation is visible in our experiments.

The pitch of C8-tolane compound has been measured as a function of temperature [33]. The helical sense reverses between the ferroelectric and antiferroelectric phases. The highest pitch is −0.6 μm in the antiferroelectric phase. Hence it is unlikely that even in our thinnest sample there would be a full unwinding of the helix. However, for thin cells, the surface anchoring of the director which suppresses the helical arrangement near the glass plates effectively enhances the electrooptic effect. It is interesting to note that when we performed these measurements, none of the earlier studies on thicker samples were able to detect the electrooptic signal deep in the antiferroelectric phase, and hence the high frequency relaxation in the SmC_A^* and SmI_A^* phases was a new result at that time. Later many others have confirmed the existence of this high frequency mode in the antiferroelectric phase mainly using dielectric measurements [63].

The electrooptic response on the same compound was also measured by Gisse et al. [73] on a **23** μm thick sample. They argue that the strongest peak (see Fig. **6.7**) is within the SmC_β^* phase rather than at the transition point between SmC_β^* and SmC_α^* phases and corresponds to a minimum in the Goldstone mode relaxation frequency which they have measured. We have not made any frequency dependent measurements in the SmC_β^* phase. They also observed a fairly sharp peak at the SmC_β^* - SmC_γ^* transition while we see only a sharp change in the slope which probably occurs in the SmC_γ^* range. Further, they mention that below 93°C in the antiferroelectric phase of the C8-tolane compound they could not observe any relaxation in the dielectric constant between dc and 1 MHz.

$$\underset{\text{(a)}}{E = 0} \qquad \underset{\text{(b)}}{\otimes\ E} \qquad \underset{\text{(c)}}{\odot\ E}$$
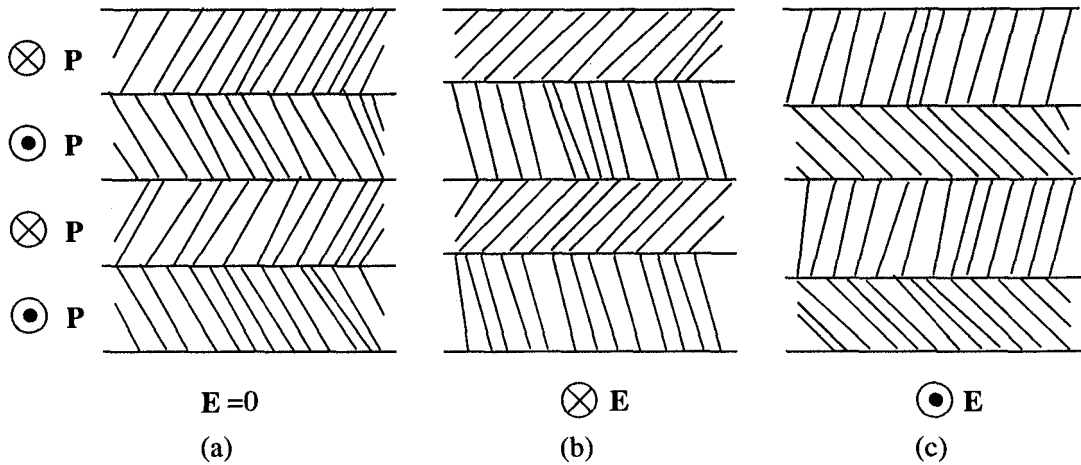
Fig. 6.13: Proposed model for the soft mode in the SmC_A^* phase which can give rise to the high frequency relaxation. (left): the symmetric tilt of the molecules in successive layers for zero field; (middle): the asymmetric tilt of the molecules in successive layers for one sign of the electric field applied normal to the plane of the paper; (right): the asymmetric tilt for the opposite field compared to the previous case.

We attribute the high frequency relaxation which we have observed in the antiferro-electric phase to a *soft* mode involving variations of the tilt angle. As the polarization directions in neighbouring layers are anti-parallel, an external field can be expected to produce an asymmetric change in the tilt angles due to the electroclinic effect (Fig. 6.13). We feel that this mode can be easily excited in the antiferroelectric phase, as in a linear approximation the changes in the tilt angle and hence in the layer thickness of neighbouring layers are equal, but opposite, *i.e.,* there is no net change in the thickness of a *pair* of layers. Hence the elastic energy associated with this mode will be much lower than the bulk compression elastic energy.

If the tilt angle in the field free case is θ_o and $\Delta\theta$ is the additional tilt introduced by the field, taking into account the fact that both θ_o and $\Delta\theta$ have opposite signs in successive layers, the transmission coefficient in the experimental geometry is given by

$$I = I_o + eE(0.707)\sin 2\theta_o \tag{6.3}$$

where e is an *electroclinic* coefficient, and I, is the transmitted intensity in the absence of the field $\vec{E}$. Since $I - I$, changes sign with that of $\vec{E}$, we get an electrooptic signal at the frequency of the applied field.

For the interpretation of the above experimental results, the appropriate dynamical equations governing the system under an ac field have to be solved. However, when we undertook the experiments, though the structure of the antiferroelectric SmC_A^* phase was clearly established, the structure of the SmC_γ^* as well as the SmC_α^* phase were not clearly known. Moreover, we found that none of the models existing at that time accounted for the entire sequence of phases exhibited by AFLC. This actually motivated us to develop a model for the various transitions exhibited by AFLC compounds. In the previous chapters we have seen that the chiral ANNNXY model developed by us is not only able to explain
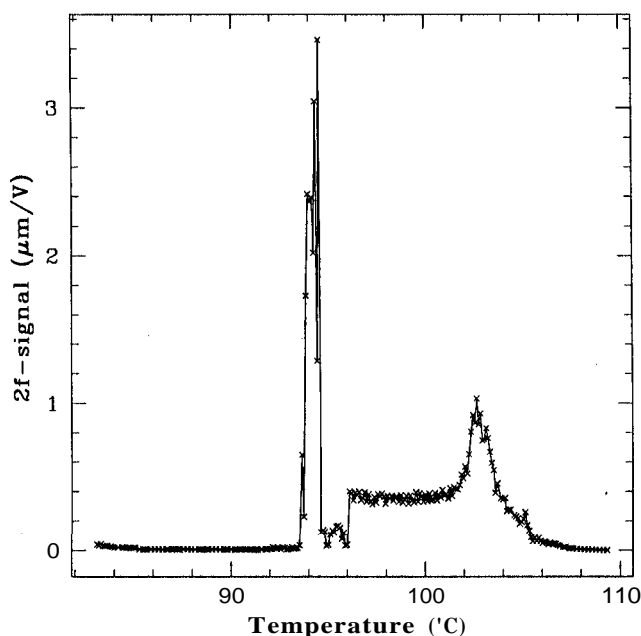
Fig. **6.14:** The temperature variation of the electrooptic 2f-response of the C8-tolane compound at 403 Hz in the homeotropic geometry. The electrode spacing used 180 μm and cell thickness is $\sim$ 30 pm.

---

the entire phase sequence but also various optical properties of the system in the presence and absence of a static electric field. However, we have not yet investigated the dynamical properties of the system in the presence of an ac field based on our model.

6.3.2   Horneotropic geometry

We have seen (Fig. 6.7) from the measurements in the honiogeneous geometry that the bounding glass plates in this geometry influence the transition temperatures. On the other hand, it is well known that the anchoring in the homeotropic alignment is such that the layer polarization is orthogonal to the surface normal and hence the influence of the surface on the phase transitions is expected to be small. However, because of the helical structure, the f-signal in this geometry is expected to be small. Therefore we have studied the temperature variation of the 2f-signal in this geometry to detect the transitions between the sub-phases. Fig. **6.14** shows a temperature run on the compound C8-tolane. The transitions between the various phases can be detected which now agree better with the DSC measurements indicating the reduced influence of the surface on the transitions. However, the data points are not as smooth as in the homogeneous geometry. The scatter in the data may arise from several reasons. As mentioned in Sec. 6.2.3, we used two flat steel wires placed parallel to each other between the glass plates for this purpose. Due to the large separation between these wires, to obtain the required electric field, a large voltage has to be applied. Moreover, this geometry gives rise to a nonuniform field within

the sample which gives rise to other complications. Though there is a relatively larger scatter in the measurements, the data serve to illustrate the fact that all the transitions can be detected even in this geometry.

6.4 Conclusions

We studied the electrooptic response of thin samples $(\sim 2-5\mu\text{m})$ of two antiferroelectric liquid crystals in the homogeneous geometry. All the transitions between the various subphases exhibited by these compounds could be very easily detected using this technique. We were able to measure an electrooptic effect for the first time in the antiferroelectric and SmI* phases of a tolane compound. We have observed a new electrooptic mode which has a relatively high relaxation frequency $(\gtrsim 100 \text{ kHz})$ in the antiferroelectric SmC_A^* phase of the C8-tolane compound. We have argued that it can arise from the electroclinic *soft* mode which produces an asymmetric tilt in successive layers of the antiferroelectric phases. These measurements motivated us to take up the theoretical studies which form the main body of this thesis.

Summary

- Our electroptic measurements are able to detect all the transitions between the subphases exhibited by antiferroelectric liquid crystals.

- We found an antiphase soft mode in the antiferroelectric SmC_A^* phase with relaxation frequency ~ 100 kHz.

- We have developed a chiral ANNNXY model for the system which takes into account the correct symmetry of order parameters in the SmC^* layers.

- Based on this model, we have calculated the phase diagrams in the appropriate parameter space which account for all the subphases for the first time.

- We have studied the influence of a static electric field on the structures of these phases. The field induces new commensurate structures in addition to the usual soliton lattice structures. The variations of the calculated apparent tilt angle with field agree well with the experimental results in different phases.

- We have simulated the conoscopic figures corresponding to these field free and field induced structures. Simulated conoscopic figures agree extremely well with the experiments. Thus the speculation that the XY-model cannot explain the conoscopic figures is incorrect.

- Our simple minded calculation of the temperature variation of ellipsometric parameters exhibits the basic features of the experimental results.

- We have also calculated the temperature variation of the optical rotatory power for this system.

- We have adapted the above model to describe the helielectric transversely polarized smectic phases which were recently discovered in compounds consisting of banana shaped achiral molecules.

References

[1] R. B. Meyer, L. Liebert, L. Strzelecki, and P. Keller, "Ferroelectric Liquid Crystals," J. Phys. (Paris) Lett. **36,** L–69 (1975).

[2] A. D. L. Chandani, Y. Ouchi, H. Takezoe, A. Fukuda, K. Terashima, K. Furukawa, and A. Kishi, "Novel Phases Exhibiting Tristable Switching," Jpn. J. Appl. Phys. **28,** L1261 (1989).

[3] A. D. L. Chandani, E. Gorecka, Y. Ouchi, H. Takezoe, and A. Fukuda, "Antiferroelectric Chiral Smectic Phases Responsible for the Tristable Switching in MHPOBC," Jpn. J. Appl. Phys. **28,** L1265 (1989).

[4] Y. Galerne and L. Liebert, "Antiferroelectric Chiral Smectic-O* Liquid Crystal," Phys. Rev. Lett. **66,** 2891 (1991).

[5] C. Bahr and D. Fliegner, "Ferroelectric-Antiferroelectric Phase Transition in a Two-Molecular-Layer Free-Standing Liquid-Crystal Film," Phys. Rev. Lett. **70,** 1842 (1993).

[6] A. Fukuda, Y. Takanishi, T. Isozaki, K. Ishikawa, and H. Takezoe, "Antiferroelectric Chiral Smectic Liquid Crystals," J. Mater. Chem. **4,** 997 (1994).

[7] V. Laux, N. Isaert, H. T. Nguyen, P. Cluzeau, and C. Destrade, "Helicity of Sc_α^* phase," Private Communication (1996).

[8] H. Takezoe, J. Lee, and A. Fukuda, "Ferrielectric Chiral Smectic Liquid Crystalline Phase," Mol. Cryst. Liq. Cryst. **202,** 85 (1991).

[9] V. Faye, J. C. Rouillon, C. Destrade, and H. T. Nguyen, "The Effect of the Position of Lateral Fluoro-Substituents on the Stability of the Sc_α^* and Sc_A^* Phases," Liq. Cryst. **19,** 47 (1995).

[10] J. Philip, J. R. Lalanne, J. P. Marcerou, and G. Sigaud, "Comparison between the SmC_α^* and SmC_γ^* Phases of MHPOBC by Optical Techniques," J. Phys. II France **4,** 2149 (1994).

[11] C. J. Booth, D. A. Dunmur, J. W. Goodby, J. Haley, and K. J. Toyne, "Achiral Swallow-tailed Materials with 'Antiferroelectric-like' Structure and Their Potential Use in Antiferroelectric Mixtures," Liq. Cryst. **20,** 387 (1996).

[12] J. Hou, J. Schacht, F. Giebelmann, and P. Zugenmaier, "Investigation on the Field-induced Switching Behaviour in an Antiferroelectric Liquid Crystal," Liq. Cryst. **22,** 401 (1997).

[13] Y. Takanishi, K. Hiraoka, V. K. Agrawal, H. Takezoe, A. Fukuda, and M. Matsushita, "Stability of Antiferroelectricity and Causes for its Appearance in SmC_α^* and SmC_A^* Phases of a Chiral Smectic Liquid Crystals, MHPOBC," Jpn. J. Appl. Phys. **30,** 2023 (1991).

[14] K. Hiraoka, Y. Takanishi, K. Skarp, H. Takezoe, and A. Fukuda, "Electric Field Induced Apparent Tilt Angle and Devil's Staircase in SmC_α^* of an Antiferroelectric Chiral Smectic Liquid Crystal," Jpn. J. Appl. Phys. **30,** L1819 (1991).

[15] E. Gorecka, A. D. L. Chandani, Y. Ouchi, H. Takezoe, and A. Fukuda, "Molecular Orientational Structures in Ferroelectric, Ferrielectric and Antiferroelectric Srnectic Liquid Crystal Phases as Studied by Conoscopic Observation," Jpn. J. Appl. Phys. **29,** 131 (1990).

[16] H. Orihara and Y. Ishibashi, "A Phenomenological Theory of the Antiferroelectric Phase Transition in Smectic Liquid Crystals," Jpn. J. Appl. Phys. **29,** L115 (1990).

[17] V. L. Lorman, A. A. Bulbitch, and P. Toledano, "Theory of Reorientational Transitions in Ferrielectric Liquid Crystals," Phys. Rev. **E49,** 1367 (1994).

[18] M. Yamashita and S. Miyazima, "Successive Phase Transitions — Ferro-, Ferri-, and Antiferro-electric Smectics," Ferroelectrics **148,** 1 (1993).

[19] M. Yamashita, "Mesophases and Ferrielectricity in the Successive Phase transition of Ferroelectric Smectic," Ferroelectrics **181,** 201 (1996).

[20] W. Selke, "The ANNNI Model- Theoretical Analysis and Experimental Applications," Phys. Rep. **170,** 213 (1988).

[21] R. Bruinsma and J. Prost, "Fluctuation Forces and the Devil's Staircase of ferroelectric Smectic C*'s," J. Phys. II (France) **4,** 1209 (1994).

[22] C. S. O. Yokoi, L. H. Tang, and W. Chou, "Ground State of the One-Dimensional Chiral XY Model in a Field," Phys. Rev. **B37,** 2173 (1988).

[23] C. Bahr, D. Fliegner, C. J. Booth, and J. W. Goodby, "Ellipsometric Study of Free-Standing Films of a Liquid Crystal Possessing Ferroelectric, Ferrielectric, and Antiferroelectric Phases," Europhys. Lett. **26,** 539 (1994).

[24] C. Bahr, D. Fliegner, C. J. Booth, and J. W. Goodby, "Experimental Indication of a Devil's Staircase Structure in a Smectic Liquid Crystal," Phys. Rev. **E51,** R3823 (1995).

[25] T. Niori, T. Sekine, J. Watanabe, T. Furukawa, and H. Takezoe, "Distinct Ferro-electric Smectic Liquid Crystals Consisting of Banana Shaped Achiral Molecules," J. Mater. Chem. **6,** 1231 (1996).

[26] T. Niori, T. Sekine, J. Watanabe, T. Furukawa, and H. Takezoe, "Distinct Ferroelectric Smectic Liquid Crystals Consisting Achiral Molecules with Banana. Shape," In Proceedings of the 16th International Liquid Crystal Conference, (1996).

[27] P. G. De Gennes and J. Prost, The Physics of Liquid Crystals, 2nd ed. (Clarendon Press, Oxford, 1993).

[28] S. Chandrasekhar, Liquid Crystals, 2nd edition ed. (Cambridge University Press, 1992).

[29] J. March, Advanced organic chemistry, fourth ed. (John Wiley & Sons, New York, 1992).

[30] G. Vertogen and W. H. deJeu, Thermotropic Liquid Crystals, Fundamentals, Vol. 45 of Springer Series in Chemical Physics (Springer-Verlag, New York, 1988).

[31] J. W. Goodby et al., Ferroelectric Liquid Crystals: Principles, Properties and Applications, Vol. 7 of Ferroelectricity and related phenomena (Gordon and Breach Science Publishers, Amsterdam, 1991).

[32] A. M. Levelut, C. Germain, P. Keller, L. Liebert, and J. Billard, "Two New Mesophases in a Chiral Compound," J. Phys. (paris) **44,** 623 (1983).

[33] P. Cluzeau, H. T. Nguyen, C. Destrade, N. Isaert, P. Barois, and A. Babeau, "New Chiral Tolane Series with Antiferroelectric Properties," Mol. Cryst. Liq. Cryst. **260,** 69 (1995).

[34] H. Sun, H. Orihara, and Y. Ishibashi, "A Phenomenological Theory of Ferroelectric and Antiferroelectric Liquid Crystals Based on a Discrete Model," J. Phys. Soc. Jap. **62,** 2706 (1993).

[35] A. Roy and N. V. Madhusudana, "A Simple Model for Phase Transitions in Antiferroelectric Liquid Crystals," Europhys. Lett. **36,** 221 (1996).

[36] T. Isozaki, T. Fujikawa, H. Takezoe, A. Fukuda, T. Hagiwara, Y. Suzuki, and I. Kawamura, "Competition Between Ferroelectric and Antiferroelectric Interactions Stabilizing Varieties of Phases in Binary Mixtures of Smectic Liquid Crystals," Jpn. J. Appl. Phys. 31, L1435 (1992).

[37] T. Isozaki, T. Fujikawa, H. Takezoe, A. Fukuda, T. Hagiwara, Y. Suzuki, and I. Kawamura, "Devil's Staircase Formed by Competing Interactions Stabilizing the Ferroelectric Smectic-C* Phase and the Antiferroelectric Smectic-C_A^* Phase in Liquid Crystalline Binary Mixtures," Phys. Rev. **B48,** 13 439 (1993).

[38] P. Bak and R. Bruinsma, "One-Dimensional Ising Model and the Complete Devil's Staircase," Phys. Rev. Lett. **49,** 249 (1982).

[39] W. Selke, "Spatially Modulated Structures in Systems with Competing Interactions," in Phase Transition and Critical Phenomena, C. Domb and J. L. Lebowitz, eds., (Academic Press, New York, 1992), Vol. 15, Chap. 1, p. 1.

2

2

[40] M. Cepic and B. Zeks, "Influence of Competing interlayer interactions on the structure of the SmC_α^* Phase," Mol. Cryst. Liq. Cryst. **263,** 61 (1995).

[41] W. H. Press, S. A. Teukolsky, W. T. Vellerling, and B. P. Flannery, Numerical Recipes in C, 2nd ed. (Cambridge University Press, 1992).

[42] S. Aubry, "The New Concept of Transitions by Breaking the Analyticity in a Crystallographic Model," in Solitons and Condensed Matter Physics, A. R. Bishop and T. Schneider, eds., (Springer-Verlag, New York, 1978), Chap. 3, p. 264.

[43] A. Banerjea and P. L. Taylor, "Devil's Staircase in a One-Dimensional Model," Phys. Rev. **B30,** 6489 (1984).

[44] in Solitons in Liquid Crystals, L. Lam and J. Prost, eds., (Springer-Verlag, New York, 1992), pp. 151,293.

[45] R. B. Meyer, "Piezoelectric effects in Liquid Crystals," Phys. Rev. Lett. **22,** 918 (1969).

[46] J. Villain and G. Mirta B., "The Devil's Staircase and Harmless Staircase: I. Oscillating Interactions through elastic Strains or Other Harmonic Fields," J. Phys. **C13,** 3117 (1980).

[47] W. Chou and R. B. Griffiths, "Ground State of One-Dimensional Systems using Effective Potentials," Phys. Rev. **B34,** 6219 (1986).

[48] H. Moritake, N. Shigeno, M. Ozaki, and K. Yoshino, "Optical and Dielectric Properties of Antiferroelectric Liquid Crystals and Their Surface Effects," Liq. Cryst. **14,** 1283 (1993).

[49] X. Y. Wang and P. L. Taylor, "Devil's Staircase, Critical Thickness, and Propagating Fingers in Antiferroelectric Liquid Crystals," Phys. Rev. Lett. **76,** 640 (1996).

[50] C. Y. Young, R. Pindak, N. A. Clark, and R. B. Meyer, "Light-Scattering study of Two-Dimensional Molecular-Orientation Fluctuations in a Freely suspended Ferroelectric Liquid Crystal Film," Phy. Rev. Lett. **40,** 773 (1978).

[51] S. Teitler and B. W. henvis, "Refraction in Stratified, Anisotropic Media," J. Opt. Soc. Am. **60,** 830 (1970).

[52] W. Berreman, "Optics in Stratified and Anisotropic Media: 4×4-Matrix Formulation," J. Opt. Soc. Am. **62,** 502 (1972).

[53] M. Born and E. Wolf, Principles of Optics, 2nd ed. (Pergamon, New York, 1970).

[54] K. Eidner, "Light Propagation in a Stratified Media: Orthogonality and Symmetry properties of the 4 x 4 matrix formalism," J. Opt. Soc. Am. **A6,** 1657 (1989).

[55] R. M. A. Azzam and N. M. Bashara, *Ellipsometry and* Polarized Light (North-Holland, Amsterdam, 1989).

[56] H. Furue, H. Uehara, J. Hatano, H. Saito, S. Saito, and E. Okabe, "Optical Activity in Antiferroelectric Liquid Crystals," Jpn. J. Appl. Phys. 36, **5046 (1996).**

[57] G. Ayton, M. J. P. Gingras, and G. N. Patey, "Orientational Ordering in Spatially Disordered Dipolar Systems," Phys. Rev. Lett. **75, 2360** (1995).

[58] **J. Prost, R.** Bruinsma, and F. Tournilhac, "Theory of Longitudinal Fesroelectric Smectics," J. Phys. II (France) **4, 169 (1994).**

[59] F. Tournilhac, L. M. Blinov, J. Simon, and S. Y. Yablonsky, "Ferroelectric Liquid Crystals from Achiral Molecules," Nature 359, **621 (1992).**

[60] Y. Shi, F. G. Tournilhac, and S. Kumar, "Bilayer Smectic Order in a Mixture of Polyphilic Liquid Crystals," Phys. Rev. **E55, 4382 (1997).**

[61] T. Selkine, T. Niori, J. Watanabe, T.Furukawa, S. W. Choi, and H. Takezo, "Spontaneous Helix Formation in Smectic Liquid Crystals Comprising Achiral Molecules,", J. Mater. Chem., **1997,** in press.

[62] H. Takezoe, A. Fukuda, A. Ikeda, Y. Takanishi, T. Uniemoto, J. Watanabe, H. Iwane, M. Hata, and K. Itoh, "On the Appearance of the Antiferroelectric Phase," Ferroelectrics **122, 521 (1991).**

[63] J. Hou, J. Schacht, F. Giebelmann, and P. Zugenmaier, "Temperature and Bias-Field Dependences of Dielectric Behaviour in the Antiferroelectric Liquid Crystal, (R)-MHPOBC," Liq. Cryst. 22, **409 (1997).**

[64] **M.** Buivydas, F. Gouda, S. T. Lagerwall, and B. Stebler, "The Molecular Aspects of the Double Absorption Peak in the Dielectric Spectrum of the Antiferroelectric Liquid Crystal Phase," Liq. Cryst. **18, 879 (1995).**

[65] K. Hiraoka, A. D. L. Chandani, E. Gorecka, Y. Ouchi, H. Takezoe, and A. Fukuda, "Electric-Field-Induced Transitions among Antiferroelectric, Ferrielectric and Ferroelectric Phases in a Chiral Smectic MHPOBC," Jpn. J. Appl. Phys. **29, L1473 (1990).**

[66] **K.** Gouda, K. Skarp, and S. T. Lagerwall, "Dielectric Studies of the Soft Mode and Goldstone Mode in Ferroelectric Liquid Crystals," Ferroelectrics **113, 165 (1991).**

[67] H. Moritake, Y. Uchiyama, K. Myojin, M. Ozaki, and K. Yoshino, "Dielectric properties in the Antiferroelectric Liquid Crystals and Their DC Bias Effect," Ferroelectrics **147, 53 (1993).**

[68] **K.** Hiraoka, H. Takezoe, and A. Fukuda, "Dielectric Relaxation Modes in the Antiferroelectric Smectic C_A^* Phase," Ferroelectrics **147, 13 (1993).**

[69] S. Garoff and R. B. Meyer, "Electroclinic Effect at the A-C phase change in a Chiral Smectic Liquid Crystal," Phys. Rev. Lett. **38, 848 (1977).**

[70] K. Hiraoka, Y. Uematsu, H. Takezoe, and A. Fukuda, "Molecular Fluctuations in Smectic Phases Possessing Antiferroelectric Ordering," Jpn. J. Appl. Phys. 35, **6157 (1996).**

[71] M. Glogarova, **H.** Sverenyak, H. T. Nguyen, and C. Destrade, "Dielectric and electrooptical study of a new antiferroelectric liquid crystal with the thiobenzoate group," Ferroelectrics **147, 43 (1993).**

[72] M. Glogarova, **H.** Sverenyak, A. Fukuda, and H. Takezoe, "Electrooptic Properties of Chiral Smectic Liquid Crystals with a Dipolar Order," Liq. Cryst. **14, 463 (1993).**

[73] P. Gisse, J. Pavel, H. T. Nguyen, and V. L. Lorman, "Dielectric Permittivity of Antiferroelectric Liquid Crystals," Ferroelectrics **147, 27 (1993).**

[74] J. Li, **H.** Takezoe, and A. Fukuda, "Novel Temperature Dependences of Helical Pitch in Ferroelectric and Antiferroelectric Chiral Smectic Liquid Crystals," Jpn. J. Appl. Phys. **30, 532 (1991).**

[75] **T.** Povse, J. Musevic, B. Zeks, and R. Blinc, "Phase Transitions in Ferroelectric Liquid Crystals in a Restricted Geometry," Liq. Cryst. **14, 1587 (1993).**